

Momentum mapping of continuum electron wave packet interference

Weifeng Yang,¹ Huatang Zhang,¹ Cheng Lin,¹ Jingwen Xu,¹ Zhihao

Sheng,¹ Xiaohong Song,^{1,*} Shilin Hu,^{2,3} and Jing Chen^{2,3,†}

¹*Department of Physics, College of Science, Shantou University, Shantou, Guangdong 515063, China*

²*CAPT, HEDPS, and IFSA Collaborative Innovation Center of MoE*

College of Engineering, Peking University, Beijing 100084, China

³*Institute of Applied Physics and Computational Mathematics, P. O. Box 8009, Beijing 100088, China*

(Dated: August 18, 2016)

We analyze the two-dimensional photoelectrons momentum distribution of Ar atom ionized by midinfrared laser pulses and mainly concentrate on the energy range below $2U_p$. By using a generalized quantum trajectory Monte Carlo (GQTMC) simulation and comparing with the numerical solution of time-dependent Schrödinger equation (TDSE), we show that in the deep tunneling regime, the rescattered electron trajectories plays unimportant role and the interplay between the intra-cycle and inter-cycle results in a ring-like interference pattern. The ring-like interference pattern will mask the holographic interference structure in the low longitudinal momentum region. When the nonadiabatic tunneling contributes significantly to ionization, i.e., the Keldysh parameter $\gamma \sim 1$, the contribution of the rescattered electron trajectories become large, thus holographic interference pattern can be clearly observed. Our results help paving the way for gaining physical insight into ultrafast electron dynamic process with attosecond temporal resolution.

PACS numbers: 32.80.Wr, 33.60.+q, 61.05.jp

I. INTRODUCTION

Atomic photoionization under intense laser irradiation is a fundamental process in strong-field light-matter interaction. The physical picture is understood by the simple man's model [1]. Within this model, the electron is released first from its parent atomic core by ionization, then is accelerated in the laser field and redirected to the parent ion, and finally re-collides with the parent ion. Usually, the ionization process is divided into two regimes: multiphoton ionization and tunneling ionization. The Keldysh parameter, $\gamma = \sqrt{\frac{I_p}{2U_p}}$ (I_p is the ionization potential, and $U_p = \frac{I}{4\omega^2}$ denotes the ponderomotive energy, where I is the laser intensity and ω is the angular frequency), is an indicator as to distinguishing these two ionization regimes [2]. When γ is much less than 1, the ionization process is in the tunneling regime, where quasi-static approximation is valid. When γ is much larger than 1, it is in the multiphoton ionization regime. When $\gamma \sim 1$, it is considered to be a transition from the tunneling regime to the multiphoton regime, and the barrier in the combined Coulomb and laser field potential changes significantly during tunneling [3].

Interference is a very important concept of coherent matter waves which has been extended successfully to explore highly nonlinear quantum-mechanical phenomena in strong-field light-matter interaction. The interference of the two electron wave packets (EWPs) ionized with exactly one optical cycle relative delay reaching the same final momentum gives rise to above-threshold ionization (ATI) rings, i.e., the intercycle interference, that are spaced by the energy of one photon in photoelectron spectrum. In addition to the intercycle interference, a

temporal double-slit pattern can be verified as signature of EWP interference emitted from the successive maxima of the absolute value of the electron field, which is the intracycle interference [4, 5]. The interference pattern of the interplay between intra- and intercycle interferences in multicycle photoelectron spectra has been identified as diffraction pattern for a time grating [5–9]. Recently, a holographic structure has been observed in photoionization and it is demonstrated to be the interference between the direct and rescattered EWPs ionized within the same quarter-cycle of the laser pulse [10–15]. In the total photoelectron momentum distribution spectrum, all these interference processes will interplay with each other, and various interference patterns will mix together. As a result, establishing an unambiguous one-to-one relationship between certain interference pattern and the corresponding electronic dynamic process is essential for retrieving the information of electronic dynamics from the measured photoelectron momentum spectrum.

On the other hand, with the development of intense mid-IR sources, experimental probing deep into the tunneling regime has become possible. Using a high repetition rate OPCPA, Keldysh parameters approaching $\gamma \sim 0.1$ can be achieved [16]. In this regime, unexpected low energy structure, very low energy structure, and even zero energy structure have been observed [17–20]. All these experimental results and the following theoretical analysis greatly advances people's understanding in this field. In the original paper of strong-field photoelectron holography, tunneling ionization had been assumed to be essential for the holographic interference (in that experiment, $\gamma = 0.76$) [10]. Subsequently, further investigations indicated that the holographic interference pattern can also be observed under the conditions belong to the

multiphoton regime ($\gamma > 1$) [11]. However, whether the photoelectron hologram can be observed in deep tunneling regime (i.e., $\gamma \ll 1$) has not yet been analyzed.

In the present work, we analyze the photoelectron angular distributions (PADs) in atomic ATI with midinfrared laser pulses. A profound ring-like interference pattern is identified by both of time-dependent Schrödinger equation (TDSE) and generalized quantum-trajectory Monte Carlo (GQTMC) simulations in the deep tunneling regime. Within the description of the QTMC, the ring-like interference pattern is demonstrated to be the superposition between the intra- and inter-cycle interference. The center of the ring-like interference pattern lies in where separations between adjacent temporal double-slit interference fringes are nearly the same as those of the ATI rings. Moreover, Coulomb potential plays a negligible role on the formation of the ring-like interference pattern. The existence of the ring-like interference pattern will mask the holographic interference pattern in the low final longitudinal momentum range, so that the holographic interference pattern can only be observed in the high final longitudinal momentum range. As a result, we identify that deep tunneling is not an appropriate condition for observing the holographic interference pattern. In the nonadiabatic regime, the contribution of the rescattering electron trajectories will increase, so the holographic interference will be clearly observed.

This paper is organized as follows. In Sec. II we introduce the theoretical methods including the numerical solutions of the TDSE and the QTMC model. In Sec. III, firstly, we show different characteristics of the interference structures in PADs in different laser parameter regions using the TDSE and QTMC simulations. Secondly, the underlying mechanism of the ring-like pattern is discussed based on the QTMC method. Moreover, the intra-, intercycle interference and the Coulomb potential effects on the interference pattern are discussed. We summarize our results and conclude in Sec. IV.

II. THEORETICAL MODELS

In this section, we summarize the numerical solution of the TDSE and the QTMC method. The numerical solution of the TDSE is considered to be exact and can be used as a benchmark for assessing the validity of the QTMC method.

The numerical solution of the time-dependent Schrödinger equation

We consider an atom interacting with a linearly polarized laser field within the single active electron approximation. The electric field of the laser pulse is

$$\mathbf{E}(t) = E_0 f(t) \cos(\omega t) \hat{z}, \quad (1)$$

where \hat{z} is the laser polarization direction, with $f(t)$ the pulse envelope function. E_0 is peak field strength. We solve the atomic TDSE

$$i \frac{\partial}{\partial t} \Psi(\mathbf{r}, t) = \left\{ \frac{\mathbf{p}^2}{2} + \mathbf{p} \cdot \mathbf{A}(\mathbf{t}) + \mathbf{V}(\mathbf{r}) \right\} \Psi(\mathbf{r}, t). \quad (2)$$

Here, \mathbf{p} is the momentum, $\mathbf{V}(\mathbf{r})$ is the atomic potential of Ar, $\mathbf{A}(\mathbf{t}) = -\int_0^t \mathbf{E}(t') dt'$ is the vector potential, and \mathbf{r} the position of the electron. The exact time evolution of the wave function $\Psi(t)$ is evaluated by using the split-operation method in energy representation [21, 22]. The space is split into two parts, i.e., the inner and outer region where the atomic potential becomes negligible compared to the kinetic energy. When the time-dependent wave function in space reaches the outer region, we project the outer region wave function on Volkov states to obtain the momentum distribution [13, 23].

The generalized quantum trajectory Monte Carlo method

To explore the physical reason of the TDSE results, we apply a QTMC method [15] based on the nonadiabatic ionization theory [24, 25], classical dynamics with combined laser and Coulomb fields [26–28], and the Feynman's path integral approach [29, 30]. The ionization rate is given as:

$$\Gamma(t) = N(t) \exp\left(-\frac{E_0^2 f^2(t)}{\omega^3} \Phi(\gamma(t), \theta(t))\right), \quad (3)$$

where $\theta(t)$ is the phase of the laser electric field. For convenience of analysis, the laser pulse envelope $f(t)$ is half-trapezoidal, constant for the first four cycles and ramped off linearly within the last two cycles. The preexponential factor is

$$N(t) = A_{n^*, l^*} B_{l, |m|} \left(\frac{3\kappa}{\gamma^3}\right)^{\frac{1}{2}} C I_p \left(\frac{2(2I_p)^{3/2}}{E(t)}\right)^{2n^* - |m| - 1} \quad (4)$$

$$\kappa = \ln(\gamma + \sqrt{\gamma^2 + 1}) - \frac{\gamma}{\sqrt{\gamma^2 + 1}}$$

where the coefficient A_{n^*, l^*} and $B_{l, |m|}$ coming from the radial and angular part of the wave function, are given by Eq.(2) of Ref. [24]. $C = (1 + \gamma^2)^{|m|/2 + 3/4} A_m(\omega, \gamma)$ is the Perelomov-Popov-Terent'ev correction to the quasistatic limit $\gamma \ll 1$ of the Coulomb preexponential factor with A_m given by Eqs. (55) and (56) of Ref. [25]. The tunnelled electrons have a Gaussian distribution on the initial transverse momentum $\Omega(v_r^j, t_0) \propto [v_r^j \sqrt{2I_p}/|E(t_0)|] \exp[\sqrt{2I_p}(v_r^j)^2/|E(t_0)|]$.

The coordinate of the tunnel exit shifts toward the atomic core due to the nonadiabatic effects [25], and the

tunnel exit point is

$$Z_0 = \frac{2I_p}{E(t_0)}(1 + \sqrt{1 + \gamma^2(t_0)})^{-1} \quad (5)$$

Thereafter, the classical motion of the electrons in the combined laser and Coulomb fields is governed by the Newtonian equation:

$$\frac{d^2}{dt^2}\mathbf{r} = -\mathbf{E}(t) - \nabla(V(\mathbf{r})). \quad (6)$$

According to the Feynman's path integral approach, the phase of the j th electron trajectory is given by the classical action along the trajectory

$$S_j(\mathbf{p}, t_0) = \int_{t_0}^{+\infty} \{\mathbf{v}_p^2(\tau)/2 + I_p - 1/|\mathbf{r}(t)|\} d\tau \quad (7)$$

where \mathbf{p} is the asymptotic momentum of the j th electron trajectory. The probability of each asymptotic momentum is determined by

$$|\Psi_{\mathbf{p}}|^2 = \left| \sum_j \sqrt{\Gamma(t_0, v_r^j)} \exp(-iS_j) \right|^2. \quad (8)$$

With GQTMC method, as showing in the following section, one can reproduce the TDSE results and extract all the information about the electron trajectory including the initial ionization phase and velocity. Moreover, by GQTMC method, one can reconstruct momentum distribution with the photoelectrons from special subcycle time windows, which is in favour of exploring the interference and Coulomb potential effects.

III. RESULTS AND DISCUSSION

Using the TDSE [Figs. 1 (a) and (c)] and GQTMC [Figs. 1 (b) and (d)], we have calculated PADs of ionization from Ar atom in linearly polarized laser fields with different laser parameters (1850 nm, $1.05 \times 10^{14} \text{W/cm}^2$, corresponding to $\gamma = 0.48$, and 1300 nm, $0.4 \times 10^{14} \text{W/cm}^2$, corresponding to $\gamma = 1.11$). The GQTMC simulations agree well with the TDSE results in both of the tunneling ionization regime and the transition regime. Both of the TDSE and GQTMC simulations show that, in the tunneling ionization regime, in addition to the ATI rings which center at zero, another ring-like interference pattern centers at about $p_z \sim 0.56a.u.$ and $p_r = 0$ can be clearly observed. However, in the transition regime where $\gamma \sim 1$, the ring-like interference pattern disappears, whereas the holographic “fork” interference structure can be identified in the PADs. Next we will discuss the physical mechanism of the ring-like interference pattern and the conditions required for the appearance of these different interference patterns.

With the help of the GQTMC back analysis of the PADs, we can disentangle different contributions of photoelectrons emitted from different time windows and analyze the interplay among them. We find the photoelectrons contributing to the ring-like fringes come from at least three sub-cycle time windows, which are labeled as A, B and C in Fig. 2(a). It is found that in the time windows A or B, there are two kinds of typical trajectories: the rescattering trajectory (trajectory R in Fig. 2(b)) and the so-called indirect trajectory (trajectory ID in Fig. 2(c)). The main distinction between these two kinds of trajectories lies in that the wave packet of the trajectory ID does not interact with the parent ion when it comes back close to $z = 0$. The interference between these two types of trajectories from single A or B will induce the fork-like holographic interference pattern. In window C, there is only one kind of typical trajectory: direct trajectory (trajectory D in Fig. 2(d)). It has been well-known that the intercycle interference of EWPs liberated with a relative time delay of one optical cycle (for example, the interference between EWPs coming from window A and B) will induce a series of ATI rings separated by one photon energy. While the intracycle interference of EWPs from window A and C induces a temporal double-slit interference pattern which has been studied both experimentally and theoretically [4].

Fig. 3 shows reconstructed photoelectron momentum spectra from different kinds of interference. Figs. 3(a) and (d) show the temporal double-slit interference pattern reconstructed with EWPs released from time windows A and C; Figs. 3(b) and 3(e) are the ATI interference pattern reconstructed with EWPs from time windows A and B; whereas Figs. 3(c) and (f) are photoelectron spectra reconstructed with EWPs released from all these three time windows A, B, and C. One can see that, compared with the outgoing ATI rings, the temporal double-slit interference pattern is a ring-like structure centered a much higher final momentum p_z . Moreover, the separations of neighbor ring-like fringes are unequal and, on the contrary to the ATI rings, gradually increase with energy in the momentum distribution map.

To show more clearly the influence of the Coulomb potential, we further present in Fig. 4 the results without considering the Coulomb potential. Comparing with Fig. 3, we can see that the impact of the Coulomb potential is reflected mainly in: (i) it distorts substantially the PADs in the low momentum ranges; (ii) it introduces the rescattered trajectory, i.e., the trajectory R. Without the Coulomb potential, the trajectory R will not exist, and so does the holographic interference. In both Figs. 3(a) and 3(b), the holographic interference structures can be hardly seen, which means that the contribution of trajectory R is quite small under the laser condition $\gamma = 0.48$. Most interestingly, when we reconstruct the momentum distribution of photoelectrons from all the three windows, the ring-like interference pattern comes out in both cases

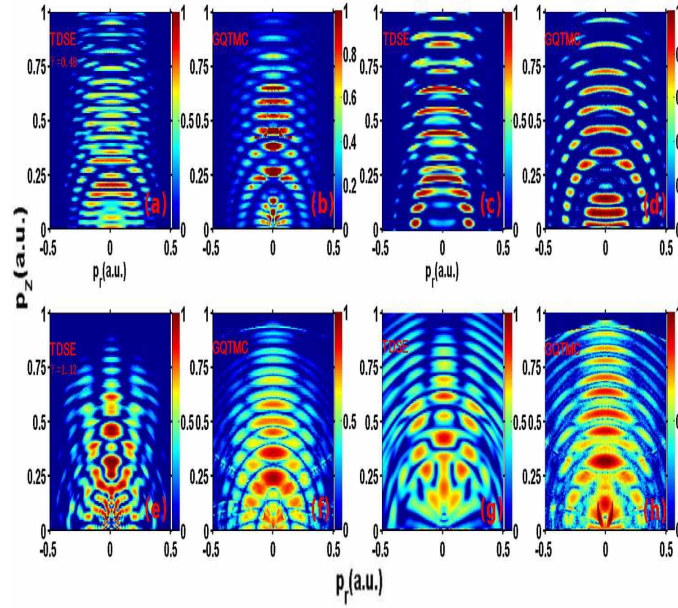


FIG. 1: (color online). Simulated two-dimensional photoelectron momentum spectra of Ar atom. Left panel: TDSE results; right panel: GQTMC simulations. (a)-(c): $\gamma = 0.55$, $I = 7.0 \times 10^{13}$ W/cm², $\lambda = 1700$ nm. (d)-(f): $\gamma = 1.11$, $I = 1.5 \times 10^{13}$ W/cm², $\lambda = 1700$ nm.

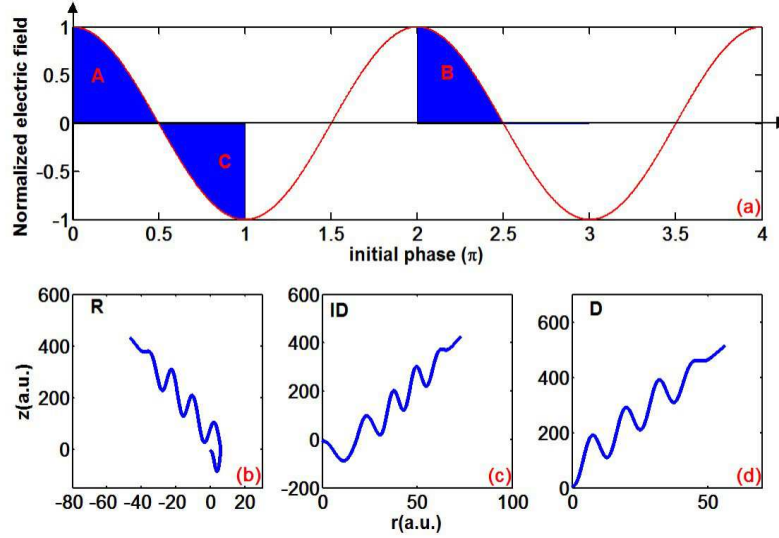


FIG. 2: (color online). Upper row (a): The electric field of laser. Lower row: (b) the collections of typical trajectory R, (c) the collections of typical trajectory ID, (d) the collections of typical trajectory D.

with and without considering the Coulomb potential (see Fig. 3(c) and Fig. 4(c)), demonstrating that the Coulomb potential and the so-induced trajectory R play a negligible role in this interference structure.

In the case of $\gamma = 1.11$, the situation is quite different. The contribution of trajectory R can already be discerned in the intracycle temporal double-slit interference structure. In the intercycle interference photoelectron momentum distribution (see Fig. 3(e)), both the fork-like holographic interference pattern along with the ATI

rings can be clearly distinguished. Remarkably different from the case of $\gamma = 0.48$, the momentum distribution of photoelectrons from these three windows cannot form a ring-like structure. On the contrary, the holographic interference structure can be clearly observed (see Fig. 3(f)). This demonstrates that the rescattered trajectory R indeed contributes importantly to holographic interference in the total photoelectron momentum distribution in this laser condition.

The above analysis can be further demonstrated by

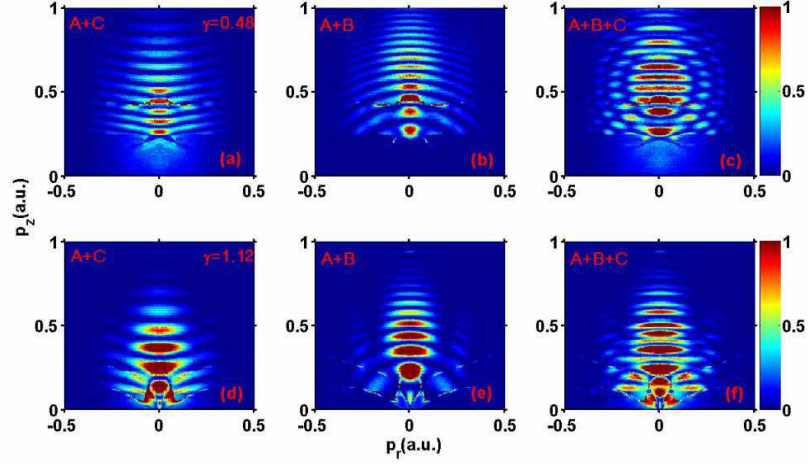


FIG. 3: (color online). Reconstructed photoelectron momentum spectra with EWPs from different time windows: (a) and (d) with EWPs from time windows A and B; (b) and (e) with EWPs from time windows A and C; (c) and (f) with EWPs from time windows A, B, and C. (a)-(c): $\gamma = 0.48$. (d)-(f): $\gamma = 1.11$.

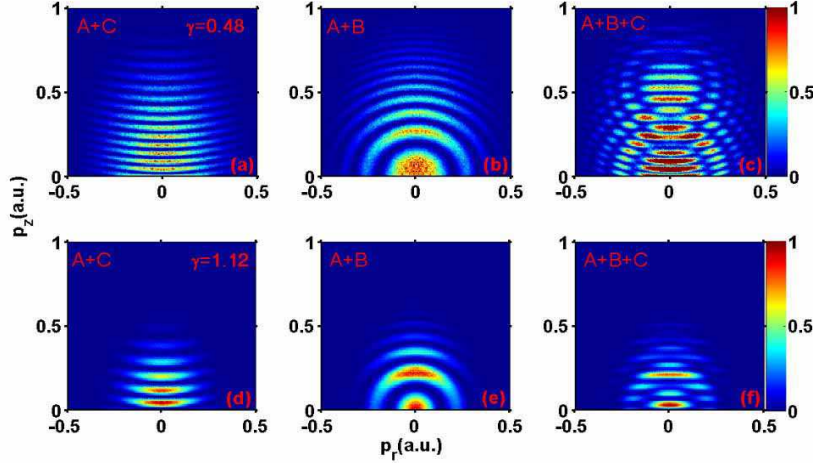


FIG. 4: (color online). Same with Fig.3 but without considering the Coulomb potential.

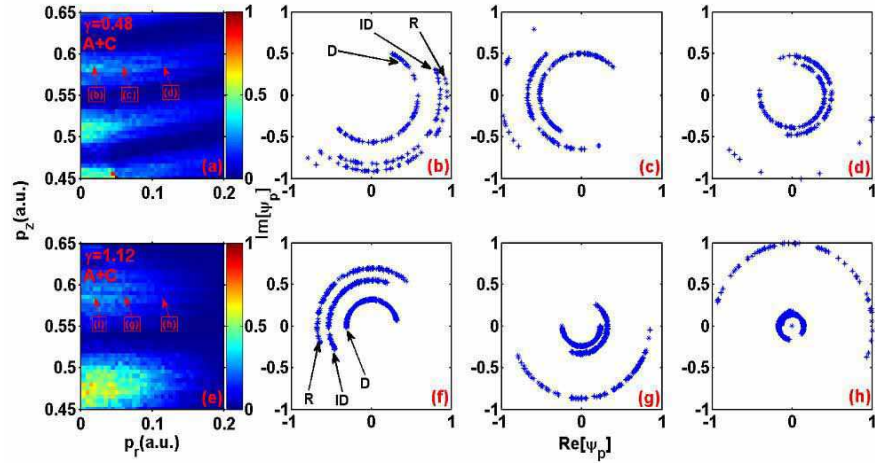


FIG. 5: (color online). (a) and (e) present zooms into Figs. 3(a) and (d) with 3 sampling points indicated. (b-d) and (f-h) show the probabilities of the summed trajectories Ψ_p in the complex plane.

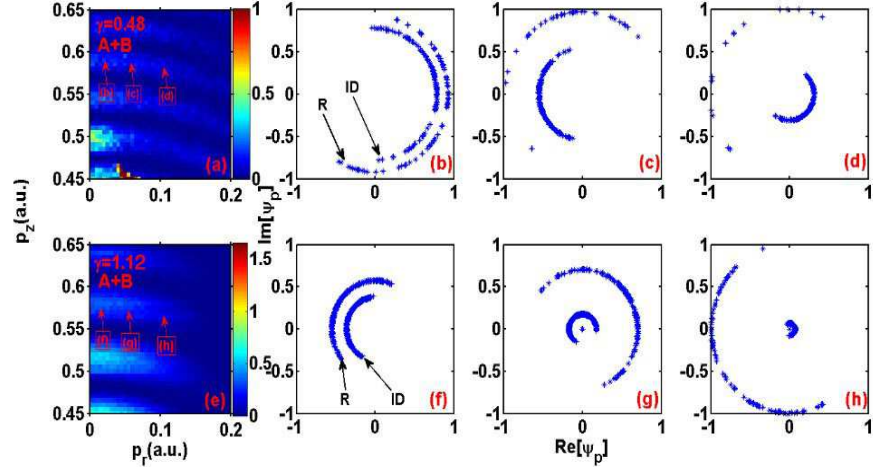


FIG. 6: (color online). Same with Fig. 5 but for three sampling points in Figs. 3(b) and (e).

the statistical trajectory-based analysis in the complex plane [31]. Figs. 5(a) and (e) present zooms into Figs. 3(a) and (d). Figs. 5(b-d) and (f-h) show the probabilities of the trajectories Ψ_p in the complex plane (the radius represents the weight $|\sqrt{\Gamma(t_0, v_r^j)}|$ and the angle represents the phase S_j of each trajectory) for 3 sampling points indicated in Figs. 5(a) and 5(e), respectively. Fig. 6 shows the same analysis but for the intracycle interference (Figs. 3(b) and (e)). It can be seen that for each sampling points in the intracycle interference pattern, there are three arcs which correspond to the three different kinds of electron trajectories (trajectories D, ID and R), whereas for intercycle interference, only two arcs corresponding trajectories D and R contribute to the interference pattern. The outermost arc corresponds to the rescattered trajectory R. When the two arcs align in the same direction, constructive interference occurs, otherwise, the opposite alignment leads to destructive interference. By comparing the two cases with different laser conditions, we can see that, for $\gamma = 0.48$, the number of the rescattered trajectory R is greatly reduced. On the contrary, for $\gamma = 1.11$, the rescattered trajectory R contributes greatly to the total momentum spectrum. As a result, holographic interference structure can be clearly distinguished from the total momentum distribution spectra (see Figs. 1(c) and (d)). All these are consistent with the above analysis. Therefore, we can conclude that the rescattered trajectory R is very vital: when the contribution of rescattered trajectory R increases, the holographic interference pattern will be clearly visible, otherwise, the ring-like interference structure will be formed due to the interplay between the intracycle and intercycle interference of direct and indirect electron trajectories.

Since the Coulomb potential plays an negligible role in the ring-like interference, to shed more light on the physical origination of the ring-like interference pattern,

our further analysis will be based on our GQTMC simulations without considering the Coulomb potential. Figs. 7(a),(b) and (c) show the temporal double-slit interference patterns, ATI rings, and the total momentum distribution spectrum, respectively. The red lines indicate the momentum spectrum for $p_r = 0$. We find that at small momentum range (i.e., $p_z < 0.56a.u.$), the separations between adjacent temporal double-slit interference fringes are smaller than those of the ATI rings, as a result, the total photoelectron spectrum clearly shows the modulation of the intracycle double-slit interference by the intercycle interference. At around $p_z \sim 0.56a.u.$, the separations between adjacent temporal double-slit interference fringes are nearly the same as those of the ATI rings. In the total momentum distribution spectrum, this forms the center of the ring-like interference pattern. Above this momentum region, the separations of temporal double-slit interference fringes are larger than those of the ATI fringes, so the double-slit interference fringes are imprinted a modulation envelope of the ATI fringes. We collect the phases of indirect and direct electron trajectories from time windows A and B resulting in the ring-like pattern, and found that the phase difference between electron trajectories from A and B is approximately equal to that from A and C, which confirms the above analysis of Fig. 7. In ref.[6], it has been shown through a 1D “simple man’s” model that the energy separation between adjacent peaks will reach a maximum and then decrease with increasing photoelectron energy. It means that with increasing p_z , there will be more than one chance that the separations between adjacent fringes for the two interference processes become nearly the same, and so there would be more than one ring-like interference structures in the total momentum distribution spectrum if the scattered trajectory R do not contribute significant.

In Fig. 8, we further show the TDSE simulation with

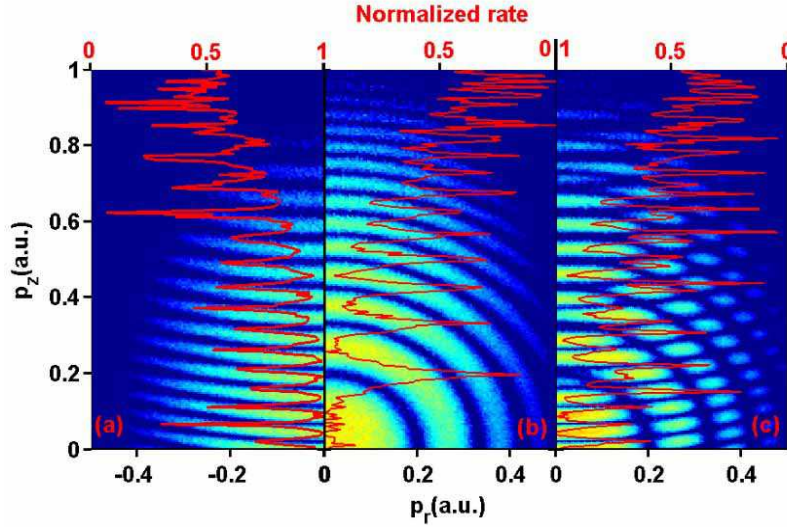


FIG. 7: (color online). (a) temporal double-slit interference pattern, (b) ATI rings, (c) the total momentum distribution spectrum reconstructed with EWPs from three time windows A, B and C. The red lines indicate the momentum spectrum for $p_r = 0 a.u.$

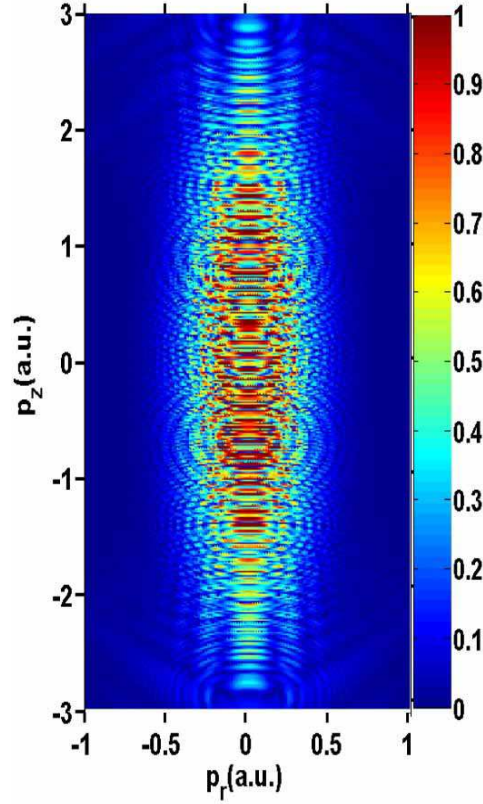


FIG. 8: (color online). TDSE simulation in deep tunneling regime: $\gamma = 0.28$, $I = 2.76 \times 10^{14} \text{ W/cm}^2$, $\lambda = 2000 \text{ nm}$.

laser conditions of $\gamma = 0.28$ which is in the deep tunneling regime. It can be seen that below $p_z \sim 2 a.u.$, there are several ring-like interference structures, which means that the direct and indirect electron trajectories play a dominant role on the total momentum distribution spectrum, and the interplay between the intracycle and in-

tercycle interferences induces these ring-like interference patterns. Such ring-like interference pattern will blur the fork-like holographic interference structure which can only be clearly visible at larger p_z .

IV. CONCLUSION

In conclusion, we have theoretically investigated 2D photoelectron momentum distributions in different Keldysh parameter regimes. We found in deep tunneling regime, profound ring-like interference pattern can be observed. We have identified that the ring-like interference pattern is induced by the interplay between the intra- and inter-cycle interference of electron trajectories. The center of the ring-like interference pattern lies in where separations between adjacent temporal double-slit interference fringes are nearly the same as those of the ATI fringes, which records electron dynamic information on attosecond sub-cycle resolution. The appearance of ring-like interference pattern implies that the rescattered electrons play a negligible role. The holographic interference pattern can only be visible at larger p_z , where the contribution of the rescattered electrons can be discerned. In the nonadiabatic tunneling regime, the effect of Coulomb potential will increase, so the contribution of the rescattered electron trajectories will increase, and the holographic interference pattern can be clearly distinguished. Our results indicate that the deep tunneling is not a appropriate condition for observation of the holographic interference which is more clearly visible near the nonadiabatic regime.

ACKNOWLEDGMENT

We benefited from discussions with X. Liu and X. Xie. The work was supported by the National Basic Research Program of China Grant (No. 2013CB922201), the NNSF of China (Grant Nos. 11374202, 11274220, 11274050, 11334009 and 11425414), Guangdong NSF (Grant No. 2014A030311019), and the Open Fund of the State Key Laboratory of High Field Laser Physics (SIOM). W. Y. is supported by the “YangFan” Talent Project of Guangdong Province.

* Electronic address: songxh@stu.edu.cn

† Electronic address: chen_jing@iapcm.ac.cn

- [1] P. B. Corkum, Phys. Rev. Lett. **71**, 1994 (1993).
- [2] L. V. Keldysh, Sov. Phys. JETP. **20**, 1307-1314 (1965).
- [3] M. Yu. Ivanov, M. Spanner, and O. Smirnova, J. Mod. Opt. **52**, 165 (2005).
- [4] F. Lindner *et al.*, D. B. Milošević, D. Bauer, W. Becker, and G.G. Paulus, Phys. Rev. Lett. **95**, 040401 (2005).
- [5] R. Gopalet *et al.*, Phys. Rev. Lett. **103**, 053001 (2009).
- [6] D. G. Arbó, K. L. Ishikawa, K. Schiessl, E. Persson, and J. Burgdörfer, Phys. Rev. A **81**, 021403(R) (2010).
- [7] D. G. Arbó, K. L. Ishikawa, K. Schiessl, E. Persson, and J. Burgdörfer, Phys. Rev. A **82**, 043426 (2010).
- [8] X. Xie, S. Roither, D. Kartashov, E. Persson, D. G. Arbó, L. Zhang, S. Gräfe, M. S. Schöffler, J. Burgdörfer, A. Baltuška, and M. Kitzler, Phys. Rev. Lett. **108**, 193004 (2012).
- [9] T. Remetter, P. Johnsson, J. Mauritsson, K. Varjú, Y. Ni, F. Lépine, E. Gustafsson, M. Kling, J. Khan, R. López-Martens, K. J. Schafer, M. J. J. Vrakking, and A. L’Huillier, Nat. Phys. **2**, 323 (2006).
- [10] Y. Huismans, A. Rouzée, A. Gijsbertsen, J. H. Jungmann, A. S. Smolkowska, P. S. W. M. Logman, F. Lépine, C. Cauchy, S. Zamith, T. Marchenko, J. M. Bakker, G. Berden, B. Redlich, A. F. G. van der Meer, H. G. Muller, W. Vermin, K. J. Schafer, M. Spanner, M. Yu. Ivanov, O. Smirnova, D. Bauer, S. V. Popruzhenko, and M. J. J. Vrakking, Science **331**, 61 (2011).
- [11] T. Marchenko, Y. Huismans, K. J. Schafer, and M. J. J. Vrakking, Phys. Rev. A **84**, 053427 (2011).
- [12] D. D. Hichstein *et al.*, Phys. Rev. Lett. **109**, 073004 (2012).
- [13] W. Yang *et al.*, Opt. Express **22**, 2519 (2014).
- [14] M. Meckel *et al.*, Nature Phys. **10**, 594 (2014).
- [15] X. Song, C. Lin, Z. Sheng, P. Liu, Z. Chen, W. Yang, S. Hu, C. D. Lin, and J. Chen, Sci. Rep. **6**, 28392 (2016).
- [16] M. G. Pullen *et al.*, J. Phys. B: At. Mol. Opt. Phys. **47**, 204010 (2014).
- [17] C. I. Blaga *et al.*, Nat. Phys. **5**, 335 (2009).
- [18] W. Quan *et al.*, Phys. Rev. Lett. **103**, 093001 (2009).
- [19] C. Wu *et al.*, Phys. Rev. Lett. **109**, 043001 (2012).
- [20] J. Dura *et al.*, Sci. Rep. **3**, 2675 (2013).
- [21] X. M. Tong and S. I. Chu, Chem. Phys. **217**, 119 (1997).
- [22] W. Yang, X. Song, and Z. Chen, Opt. Express **20**, 12067 (2012).
- [23] X. Tong, K. Hino, and N. Toshima, Phys. Rev. A **74**, 013405(R) (2006).
- [24] G. L. Yudin and M. Yu. Ivanov, Phys. Rev. A **64**, 013409 (2001).
- [25] A. M. Perelomov, V. S. Popov, and M. V. Terent’ev, Zh. Éksp. Teor. Fiz. **50**, 1393 (1966) [Sov. Phys. JETP **23**, 924 (1966)].
- [26] T. Brabec, M. Y. Ivanov, and P. B. Corkum, Phys. Rev. A **54**, R2551 (1996).
- [27] B. Hu, J. Liu, and S. G. Chen, Phys. Lett. A **236**, 533 (1997).
- [28] J. Chen, J. Liu, and S. G. Chen, Phys. Rev. A **61**, 033402 (2000).
- [29] P. Salières, B. Carrè, L. Le Dèroff *et al.*, Science **292**, 902 (2001).
- [30] M. Li *et al.*, Phys. Rev. Lett. **112**, 113002 (2014).
- [31] T.-M. Yan, S. V. Popruzhenko, and D. Bauer, in Progress in *Ultrafast Intense Laser Science*, edited by K. Yamanouchi, K. Midorikawa (Springer-Verlag, Heidelberg, 2013).